

Article

Not peer-reviewed version

Seismicity Before and After the 2023 *M*7.7 and *M*7.5 Turkey Earthquakes

[K. Z. Nanjo](#)^{*}, [T. Kumazawa](#), [J. Izutsu](#), [T. Hori](#), T. Nagao, K. Oike

Posted Date: 18 February 2025

doi: 10.20944/preprints202502.1352.v1

Keywords: seismicity; earthquake interaction; crustal deformation; faulting; statistical methods; *b*-value



Preprints.org is a free multidisciplinary platform providing preprint service that is dedicated to making early versions of research outputs permanently available and citable. Preprints posted at Preprints.org appear in Web of Science, Crossref, Google Scholar, Scilit, Europe PMC.

Copyright: This open access article is published under a Creative Commons CC BY 4.0 license, which permit the free download, distribution, and reuse, provided that the author and preprint are cited in any reuse.

Article

Seismicity Before and After the 2023 $M7.7$ and $M7.5$ Turkey Earthquakes

K. Z. Nanjo ^{1,2,3,4,*}, T. Kumazawa ³, J. Izutsu ^{1,5}, T. Hori ^{1,4}, T. Nagao ^{1,6} and K. Oike ¹

¹ Global Center for Asian and Regional Research, University of Shizuoka, 3-6-1 Takajo, Aoi-ku, Shizuoka 420-0839, Japan

² Center for Integrated Research and Education of Natural Hazards, Shizuoka University, 836 Oya, Suruga-ku, Shizuoka 422-8529, Japan

³ Institute of Statistical Mathematics, 10-3 Midori-cho, Tachikawa, Tokyo 190-8562, Japan

⁴ Japan Agency for Marine-Earth Science and Technology, Yokohama Institute for Earth Sciences, 3173-25 Showa-machi, Kanazawa-ku, Yokohama, Kanagawa 236-0001, Japan

⁵ International Digital Earth Applied Science Research Center, Chubu University, 1200 Matsumoto-cho, Kasugai, Aichi 487-8501, Japan

⁶ Institute of Oceanic Research and Development, Tokai University, 3-20-1 Orido, Shimizu-ku, Shizuoka 424-8610, Japan

* Correspondence: nanjo@u-shizuoka-ken.ac.jp

Abstract: A magnitude (M) 7.7 earthquake struck on February 6, 2023 in Turkey. Nine hours later, a $M7.5$ earthquake occurred near the initial $M7.7$ quake. We studied seismicity before and after these doublet quakes, integrating physics-based and statistical approaches. We first used the statistical Epidemic-Type Aftershock Sequence (ETAS) and the Bayesian Gutenberg-Richter b -value models to confirm previously-reported seismicity transients (seismic activation and low b -values) prior to the future $M7.7$ quake. We then showed that the low b -value area coincided with a high-slip area on the strand segment from which the $M7.7$ rupture started, a similar result to that obtained for the 2011 Tohoku megaquake case in Japan. We next used the physics-based Coulomb and statistical b -value models to find which locations of the largest and second largest events in the post-doublet-quake sequence were in relatively high-stress regions and became closer to failure, as a result of the doublet quakes. We further used the ETAS model to show that this sequence is currently active, but is decaying with time. The duration of the sequence was estimated at 2.7-5.5 years, longer than previously proposed (1-2.5 years). Our result was stable because it was based on earthquake data in about 600 days, six times longer than the study period used in a previous study.

Keywords: seismicity; earthquake interaction; crustal deformation; faulting; statistical methods; b -value

1. Introduction

On February 6, 2023 (UTC), a devastating earthquake of magnitude (M) 7.7 struck the East Anatolian fault zone (EAFZ) bounding the Arabian and Anatolian tectonic plates (Figure 1). This quake, which occurred near the city of Kahramanmaraş in the Mediterranean region of Turkey, was followed about nine hours later by a $M7.5$ quake approximately 90 km to the north of the initial $M7.7$ quake. The epicenter of the $M7.5$ quake was on the Sürgü fault. The broad context of the doublet quakes (the $M7.7$ and 7.5 quakes) is that they occurred under the current tectonic stress that created the EAFZ. The EAFZ accommodates the westward movement of Turkey into the Aegean Sea. Although the relative plate motions in the region around the EAFZ are low (typically less than 10 mm/yr), even regions of slow plate motions can host extremely damaging earthquakes [1].

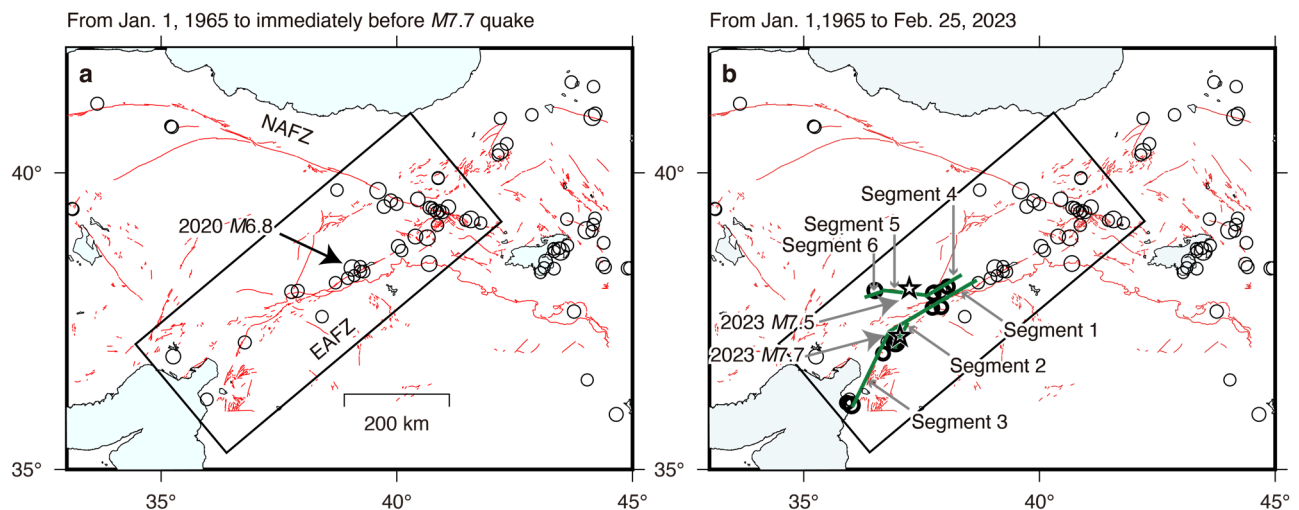


Figure 1. Seismicity around the East Anatolian fault zone (EAFZ). (a) Thin circles indicate earthquakes with $M \geq 5.5$ with a depth of 40 km or shallower during the period before the 2023 M7.7 quake, where the combined catalog was used (see the Data section). Earthquakes in the rectangular region are used for Figure 14. Red curves indicate active faults. NAFZ indicates the North Anatolian fault zone. (b) Stars indicate the M7.7 and 7.5 epicenters. Green lines show the M7.7 and 7.5 source faults [2,3]. Fault segments are numbered 1 to 6 (see the Data section). Thick circles are the same as thin ones for the period after the M7.7 quake.

During the 20th century, much of the North Anatolian fault zone (NAFZ) ruptured from east to west in a series of M7 or larger earthquakes [1]. In this same period, seismicity along the EAFZ experienced M6 earthquakes, with most of the activity on the northern section. The activity on the southern section of the EAFZ started with the Jan. 24, 2020 M6.8 quake. Figure 1b shows how the remainder of the southern section was activated during the 2023 doublet quakes and following events, where seismicity ($M \geq 5.5$) from 1965 to the M7.7 quake (thin circles) were overlaid with seismicity after the M7.7 quake (thick circles) and fault segments of the doublet quakes (green) [2,3].

The focal mechanism of the 2020 M6.8 quake indicates faulting on a near-vertical left-lateral plane trending SW-NE [4]. A slip on this plane is consistent with the orientation of regional faults and local plate motions. The M7.7 quake involved a left-lateral strike slip along SW-NE trending faults [2]. A predominant mechanism of the M7.5 quake was a left-lateral strike-slip fault motion along SW-NE and E-W trending faults [3].

The preceding M7.7 quake promoted the subsequent M7.5 quake, largely by unclamping of stress loaded on the epicentral patch of the future rupture [5]. Chen et al. [6] also showed that the M7.5 quake was promoted by historical earthquakes and finally triggered by the M7.7 quake. As performed in several studies [5–9], it is of interest to analyze the interaction between the doublet quakes. However, this possibility is out of scope in the present study. Rather, we focused on seismicity before and after the doublet quakes.

Kwiatk et al. [10] reported seismicity transients starting approximately 8 months before the 2023 M7.7 quake. One of the main characteristics of the transients was seismic activation (see also [11]). Seismicity was composed of isolated spatiotemporal clusters near a future M7.7 epicenter. Four clusters were recognized within 50 km of the future epicenter, referred to as C1, C2, C3, and C7 [10]. Clusters C1 and C2 emerged within 8 months prior to the M7.7 quake. Clusters C2 and C7 were located on and around a fault segment (segment 2 defined in the Data section), where the M7.7 quake initiated. Cluster C7 emerged in 2017–2018. Cluster C3 was activated in 2015, 2016, and 2021. The other main characteristic was the low b -value of the Gutenberg-Richter (GR) frequency-magnitude relation of earthquakes [12]. This relation will be defined in the Method section. Clusters C1 and C2 were responsible for the low b -values [10]. The authors also showed non-Poissonian inter-event time statistics and magnitude correlations of seismicity. Local comparable seismic transients have not been observed, at least not since 2014.

Seismicity after the doublet quakes was still active. About 4500 $M \geq 3$ earthquakes occurred around the causative faults during the period since the $M7.7$ quake until Oct. 16, 2024, when we used the AFAD catalog (see the Data section). Two $M6$ -class earthquakes occurred after the doublet quakes, a $M6.4$ quake on Feb. 20, 2023 [13] and a $M5.9$ quake on Oct. 16, 2024 [14] around the south and north ends of the $M7.7$ rupture, respectively. Given that the fault end zones generally calculate increases in stress [7], the areas surrounding these $M6$ -class quakes were hypothesized to be heading toward failure, using the stress calculation. In the present study, this hypothesis was proven by using currently available earthquake data and fault models.

Although active seismicity continues, the post-doublet-quake sequence undergoes the Omori-Utsu (OU) power-law decay over time [15] (see the Method section). Toda and Stein [5] estimated the duration of the post-doublet-quake sequence to be 1-2.5 years. This duration was defined as the period of a larger occurrence rate computed from using the OU relation than that computed from using ordinary earthquakes before the 2020 $M6.8$ quake. Re-evaluation of the duration of this sequence would provide the basis of a time-dependent seismic hazard assessment along the NAFZ, because almost 1.5 years have passed since the $M7.7$ quake (as of Oct. 2024).

We studied seismicity before and after the doublet quakes, using earthquake catalogs created by the Disaster and Emergency Management Authority (AFAD), Lomax [16], and Kwiatek et al. [10], to demonstrate that the result does not depend on the choice of catalog. We first confirmed previously-reported seismicity transients during the pre-doublet-quake sequence [10], using the statistical Epidemic-Type Aftershock Sequence (ETAS [17]) and GR models. Taking both physics-based and statistical approaches, we then investigated the post-doublet-quake sequence to indicate that the two $M6$ -class quakes were promoted by the doublet quakes and to discuss a comparison between our study and a previous study [5], based on currently-observable data.

2. Methods

2.1. OU Relation and ETAS Model

Seismicity after a large earthquake is often correlated with the OU relation [15] in the time domain, given as $\lambda_{OU} = k(c+t)^{-p}$, where λ_{OU} is the number of earthquakes per unit time at t with M larger than or equal to a minimum magnitude (M_{th}), and p , c , and k are constants. The rate- and state-dependent friction law [18] assumes $p=1$ as a standard form. Variability in p is possible: $p>1$ and $p<1$ for special cases with rapidly and slowly decreasing stress, respectively. The ETAS model described below considers an earthquake sequence as a result of the onset of the OU power-law decay following each previous event.

In the framework of the ETAS model [17], all earthquakes are decomposed into Poisson background activity and clustering activity. The occurrence rate of the Poisson background activity is a constant μ . The ETAS model assumes that each earthquake is followed by earthquakes in the form of the OU relation. The rate of earthquake occurrence at t following the i -th earthquake (time t_i and magnitude M_i) is given by $v_i(t) = K_0 \exp\{\alpha(M_i - M_{th})\} (t - t_i + c)^{-p}$ for $t > t_i$, where K_0 and α are constants. The rate of occurrence of the whole earthquake series at t becomes $\lambda(t|H_t) = \mu + \sum_{S < t_i < t} v_i(t)$. The summation is performed for all i satisfying $t_i < t$. Here, H_t represents the history of occurrence times with associated magnitudes from the data $\{(t_i, M_i)\}$ before time t . The parameter set $\theta = (\mu, K_0, \alpha, c, p)$ represents the characteristics of seismic activity. The units of the parameters are day^{-1} , day^{-1} , no unit, day, and no unit, respectively. θ is given by using the maximum-likelihood estimate. AIC (Akaike Information Criterion [19]), useful for assessing the goodness of fit of the model to data, is obtained from the maximum log-likelihood and the number of adjusted parameters.

It is possible to visualize how well or poorly the ETAS model fits an earthquake sequence by comparing the cumulative number of earthquakes with the rate calculated by the model [20]. Ordinary time can be converted to transformed time in such a way that the transformed sequence follows the Poisson process (uniformly distributed occurrence times) with unit intensity (occurrence rate). Visualization can be achieved in two ways: one graph using ordinary time and the other using

transformed time. If the model presents a good approximation of observed seismicity, an overlap of both observation rate and model rate is expected.

2.2. GR Relation

The GR relation [12] is given by $\log_{10}N=a-bM$, where N is the number of earthquakes with a magnitude larger than or equal to M in the given time window, and a and b are constants. b is used to describe the relative occurrence of large and small events in the given time window (i.e., a high b -value indicates a larger proportion of small earthquakes, and vice versa) [21–25]. The b -value is calculated based on earthquakes with a magnitude above the completeness magnitude M_c , above which all events are considered to be detected by a seismic network.

The results of laboratory experiments indicated a systematic decrease in the b -value approaching the time of the entire fracture [26–28]. In this context, a decrease in b and/or low b -values have been reported for the period leading up to large-size earthquakes in Sumatra, Japan, and Chile [28–30]. Although underlying physical processes associated with the temporal changes in b remain unclear, and the role of b as a stress meter is unproven, there are indications of such processes and role from laboratory experiments [26] and numerical simulations [32]. One possible physical model showed that the decrease in b was caused by a rapid increase in shear stress, promoting micro-crack growth [26]. Another possible model showed that an increased stress level in slowly slipping parts of a fault facilitates earthquake rupture growth, resulting in the temporal decrease in b prior to a large earthquake (mainshock) [32].

2.3. Stress-Change Calculation

We used Coulomb, a graphic-rich deformation and stress-change software for earthquakes, tectonics, and volcanoes [33,34] to calculate how earthquakes promote or inhibit failure on nearby faults. Static stress changes caused by the displacement of a fault (source fault) were calculated. Displacements in the elastic half space were used to calculate the 3D strain field; this was multiplied by elastic stiffness to derive the stress changes. A typical value for Poisson's ratio ($PR=0.25$), Young's modulus ($E=8\times 10^5$ bar), and friction coefficient ($\mu=0.4$) was used in this study, resulting in a shear modulus of $G=E/[2(1+PR)]=3.3\times 10^5$ bar. The shear and normal components of the stress change were resolved on specified receiver fault planes. A receiver fault consists of planes, each characterized by specified strike, dip, and rake, on which the stresses imparted by the source faults are resolved. The Coulomb failure criterion, in which failure is hypothesized to be promoted (inhibited) when the Coulomb failure is positive (negative), was used.

3. Data

3.1. Earthquake Catalogs

For analyses of long-term seismicity (Figure 1), we created an earthquake catalog based on the ISC-GEM catalog (version 9.1, released on Jun. 27, 2022) [35–38] and the ANSS catalog [39]. The catalog we created contains earthquakes with $M\geq 5.5$ during the period Jan. 1, 1965-Dec. 31, 2018 obtained from the ISC-GEM catalog and during the period Jan. 1, 2019-Feb. 25, 2023 obtained from the ANSS catalog.

For analyses of short-term seismicity, we used three earthquake catalogs created by the Disaster and Emergency Management Authority (AFAD), Lomax [16], and Kwiatek et al. [10] to demonstrate that the result does not depend on the choice of catalog. We downloaded the catalog, including earthquakes of $M\geq 1.0$ from Jan. 1, 2014 to Oct. 16, 2024. This timing of Jan. 1, 2014 coincided with the effective incorporation of seismic stations to the generation of the local seismicity catalogue by AFAD, leading to a visible improvement of the consistency of magnitude estimates since the selected time [10]. Although we filtered out events specified as explosion, downthrow, volcanic, and unknown when downloading the catalog, it is known that it includes clusters corresponding to quarry-blast

activity [10]. In this study, the events located within areas of the quarry-blast shown in Figure 2 of Kwiatek et al. [10] were excluded from the catalog. According to Kwiatek et al. [10], the AFAD catalog has $M \geq 1.5$ within a 50 km radius from the $M7.7$ quake during a period from Jan. 1, 2023 to immediately before the $M7.7$ quake (Feb. 6, 2023).

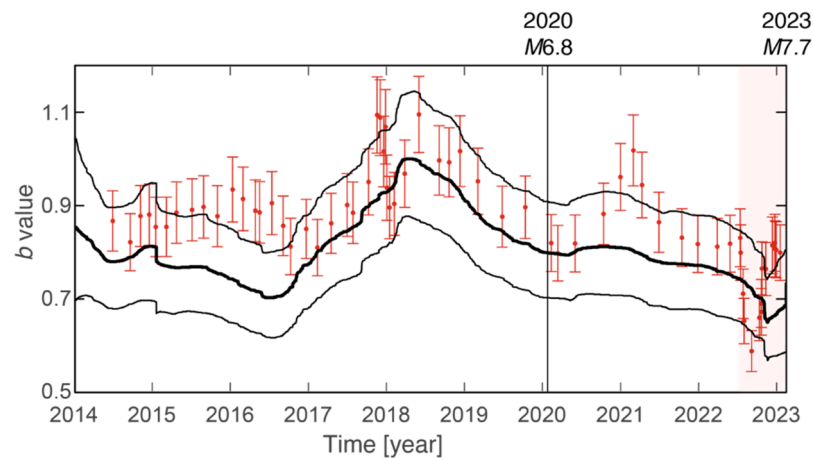


Figure 2. Timeseries of b -values in the circle with a 50-km radius centered at the $M7.7$ epicenter for the period from 2014 to immediately before the $M7.7$ quake. The circular region and the time period are the same as those used by Kwiatek et al. [10]. The b -values (with error bars showing 95% confidence interval) are shown in black curves. Also included for comparison is the time dependence of b shown in Figure 3b of Kwiatek et al. [10]. Pink region shows the period from July 1, 2022 to immediately before the $M7.7$ quake. Vertical line indicates the moment of the 2020 $M6.8$ quake.

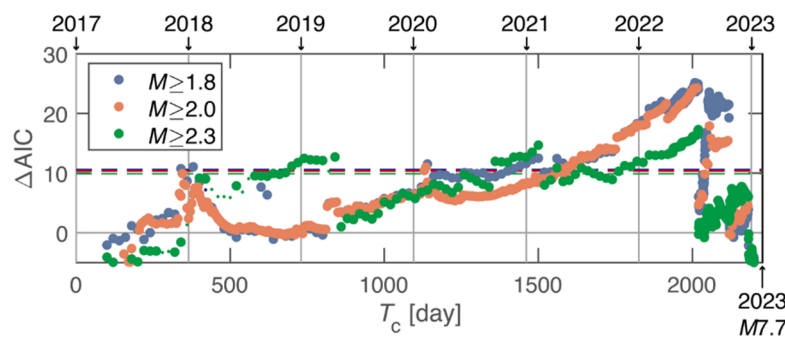


Figure 3. ΔAIC as a function of T_c for the period from Jan. 1, 2017 to immediately before the 2023 $M7.7$ quake. Blue, red, and green data are based on earthquakes of $M \geq 1.8$, 2.0, and 2.3, respectively, within a 50 km radius from the $M7.7$ epicenter. Vertical lines indicate Jan. 1, for 2018, 2019, ..., 2023. Horizontal dashed lines representing $2q$ for $M \geq 1.8$ (blue), 2.0 (red), and 2.3 (green) overlap, where q is the degree of freedom imposed when searching T_c based on the data over the entire period [45,46].

The Lomax catalog [16] (version 3.0. released on Jun. 28, 2023), which includes earthquakes from Jan. 1 to May 31, 2023, is an NLL-SSST-coherence hypocenter catalog, where NLL-SSST-coherence [40,41] is an enhanced, absolute-timing earthquake location procedure that 1) iteratively generates spatially varying travel-time corrections to improve multi-scale location precision, and 2) uses waveform similarity to improve fine-scale location precision. Relocations were performed with merged phase arrival data available from AFAD (<https://depem.afad.gov.tr/event-catalog>) and KOERI (<http://www.koeri.boun.edu.tr/sismo/2/bultenler>) [16]. All events in the AFAD catalog with $M \geq 1.5$ are used for relocation [16].

The catalog of Kwiatek et al. [10] is an enhanced seismicity catalog lowering the magnitude detection threshold around the $M7.7$ and 7.5 quakes for a period from Jan. 1, 2023 to immediately before the $M7.7$ quake (Feb. 6, 2023). This catalog was generated by using an AI-based workflow [10]. When the events located within areas identified as quarry blasts were excluded, only events

representing earthquakes remained. The catalog has $M_c=0.5$ in the 50 km radius around the $M7.7$ quake [10].

3.2. Fault Models

The fault model of the $M7.7$ quake is based on the work by the United States Geological Survey (USGS) [2]. This is a finite-fault model (also called a variable slip) with numerous small patches of slips, each having information on the location of a rectangular patch, strike, dip, and rake. The model that includes analysis of both teleseismic and regional seismic and geodetic observations represents three plane segments 1, 2, and 3, showing two main ruptures on segments 1 and 3 with one strand (segment 2) near the $M7.7$ hypocenter (Figure 1). Considering the location of the $M7.7$ hypocenter, the rupture initiated on segment 2, and the rupture radiation was bilateral along segments 1 and 3. This is consistent with the rupture model of the $M7.7$ quake [42]. A slip distribution for the rupture along segments 1 and 3 shows peak-slip values of >10 m, but along segment 2, it shows peak-slip values of about 1.5 m. The model representing the three segments involves predominantly near-vertical left-lateral strike-slip faulting.

Similarly, the finite-fault model of the $M7.5$ quake, based on work by the USGS [3], was used. This model represents three segments 4, 5, and 6 that involve predominantly near-vertical left-lateral strike-slip faulting (Figure 1). Considering the location of the $M7.5$ hypocenter, the rupture initiated on central segment 5, and the rupture radiation was bilateral along two segments (4 and 6) located at both ends of segment 5, consistent with the rupture model of the $M7.5$ quake [42]. A slip distribution for the rupture along segment 5 shows peak-slip values of >10 m, while along segments 4 and 6, it shows peak-slip values <10 m.

To calculate how the doublet quakes promoted or inhibited the $M6.4$ quake, a moment tensor solution of the $M6.4$ quake reported by the USGS [13] was used. The moment tensor contains two nodal planes (NPs). Both NPs were used as receiver faults of changes in Coulomb stress imparted by the doublet quakes. Similarly, a moment tensor solution of the $M5.9$ quake reported by the USGS [14] was used.

4. Results

4.1. Pre-Doublet-Quake Sequence

4.1.1. b-Value and Change in Seismicity Rate

We confirmed the previously-reported seismicity transients: low b -values and seismic activation starting approximately 8 months before the 2023 $M7.7$ quake in the region within a 50 km radius surrounding the future $M7.7$ epicenter [10].

We first considered unbiased time-dependent b -values (Figure 2), using our method [24] where the b -value function of time is represented by a broken line connecting the sequence of earthquakes under a smoothness constraint in piecewise slopes, using the empirical Bayesian smoothing technique. Unlike Kwiatak et al. [10], who used a moving event window of 120 events and attributed each calculated b -value to the origin time of the last event in each window, the method we used does not assume a moving window. Therefore, it has the advantage of obtaining unbiased b -values as a function of time [24]. Results (black data) based on use of the AFAD catalog show that b reached values as low as ~ 0.6 during the period from July 2022 to immediately before the $M7.7$ quake (pink region). Also included for comparison is the timeseries of b -values (red data) reproduced from Figure 3b of Kwiatak et al. [10]. Regardless of whether the previous method [10] or our method was used, the results were similar. The lowest b -values are related to two clusters, referred to as C1 and C2 by Kwiatak et al. [10].

We next showed that seismic activation, as suggested previously [10], is statistically significant, conducting a change point analysis. For this analysis, $\Delta AIC = AIC_{\text{single}} - AIC_{\text{2stage}}$ was used as a function of the change-point time T_c [20,24,43,44]. Here, AIC_{single} is AIC for the standard (single) ETAS model

that considers a constant θ -value over time, and AIC_{2stage} is AIC for the two-stage ETAS model that considers different θ -values in subperiods before and after T_c , where both models are fitted to earthquakes of $M \geq M_{th}$. If $\Delta AIC \geq 2q$, the two-stage model is better fitted to the data than the single model, detecting candidate changes in occurrence rate, where q is the degree of freedom to search for the best candidate T_c from the data. q depends on sample size (number of earthquakes of $M \geq M_{th}$) [45,46]. The result for $M_{th}=2$ (red data in Figure 3) shows that the two-stage ETAS model was much better than the single ETAS model during $T_c=1600\sim 2100$ days, where events during the period from Jan. 1, 2017 to immediately before the $M7.7$ quake in the AFAD catalog were used. The most significant T_c was 2015 days (Jul. 9, 2022). The results for $M_{th}=1.8$ (blue data) and 2.3 (green data) indicate that the most significant T_c was 2008 days (Jul. 2, 2022) and 2019 days (Jul. 13, 2022), respectively. This feature, i.e., that the most significant T_c -values are about 8 months before the $M7.7$ quake, was observed regardless of M_{th} -values.

We fitted the ETAS model to earthquakes ($M \geq 2$) before $T_c=2015$ days (Jul. 9, 2022) (Figure 4a,b). For this fitting, three time-intervals were considered [24]. One interval is called the target interval, for which θ was computed. The seismicity in this period may be affected by earthquakes which occurred before this period due to the long-lived nature represented by the OU relation. To consider this effect, another time interval, which is precursory to the target interval (called the precursory interval), was chosen and earthquakes in this period were considered in the computation. The precursory interval is defined by 0 to S . The target interval is defined by S to T . The third time interval defined by T to T_{end} is called the prediction interval. θ in this interval is the same as that computed for the target interval. We set $S=0.01$ days, $T=T_c=2015$ days (Jul. 9, 2022), and $T_{end}=2225.71$ days (immediately before the $M7.7$ quake). The occurrence rate (black) after $T=T_c=2015$ days (during the prediction interval) was larger than the extrapolated rate (red), indicating relative activation. Here, the extrapolated rate is the occurrence rate computed by using the ETAS model, in which θ was obtained by fitting to earthquakes ($M \geq 2$) before $T=T_c=2015$ days (the target interval).

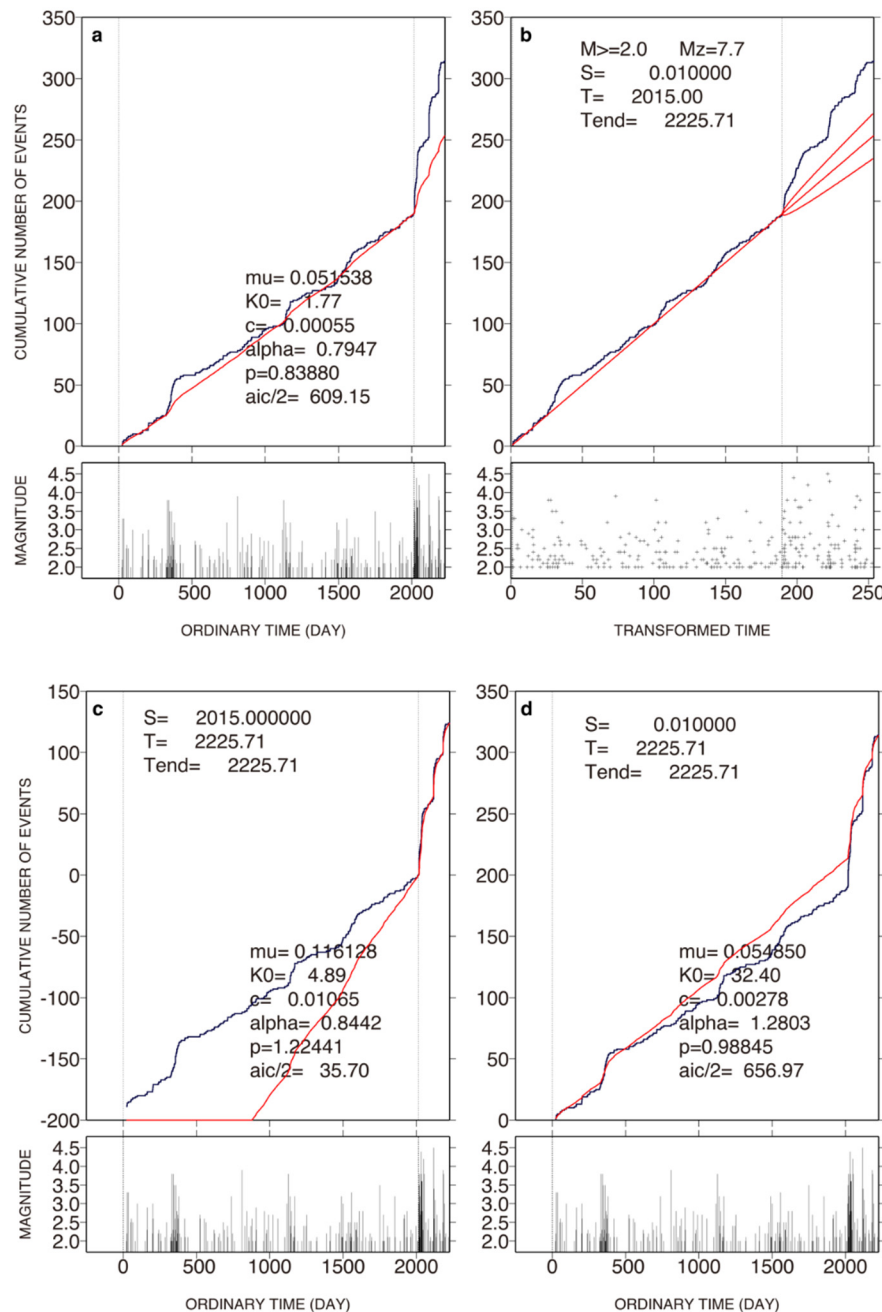


Figure 4. Change point analysis. Cumulative function of $M \geq 2.0$ earthquakes is plotted against ordinary time in **a** and transformed time in **b**, showing the ETAS fitting in the target interval from 2017 to Jul. 9, 2022 (the most significant $T_c = 2015$ days for $M \geq 2.0$ shown in Figure 3) and then extrapolated until immediately before the 2023 $M7.7$ quake. The parabola represents the 95% confidence intervals of the extrapolation [20,24,43]. The smaller panel below each larger panel indicates an M -time diagram. Because K_0 differs depending on reference magnitude M_z [20], we used $M_z = 7.7$. This value ($M_z = 7.7$) is the largest magnitude in this study. (c) As in **a** except that the target is the later time interval after Jul. 9, 2022. (d) As in **a** except that the target is the entire time interval.

4.1.2. Background Activity and Clustering Activity

We further analyzed seismicity during the 8 months before the 2023 $M7.7$ quake to explore the reason for the change in the rate of earthquake occurrence (Figure 5). We took a reductionism approach, by decomposing all earthquakes into Poisson background activity and clustering activity. We measured μ (a solo parameter of the Poisson background activity) and K_0 (a parameter representing the clustering activity), where the other three parameters (α , c , p) were constants. We used a non-stationary ETAS approach [24,43,46,47] to seismicity before the $M7.7$ quake. The standard (single) ETAS model, which is the stationary ETAS model, can be temporally extended to the non-

stationary ETAS model in such a way that μ and K_0 are assigned as a function of t . The function $\mu(t)$ is represented by a broken line connecting the sequence $(t_i, \mu(t_i))$ for the i -th earthquake, using a Bayesian function. Similarly, $K_0(t)$ is represented by a broken line connecting the sequence $(t_i, K_0(t_i))$.

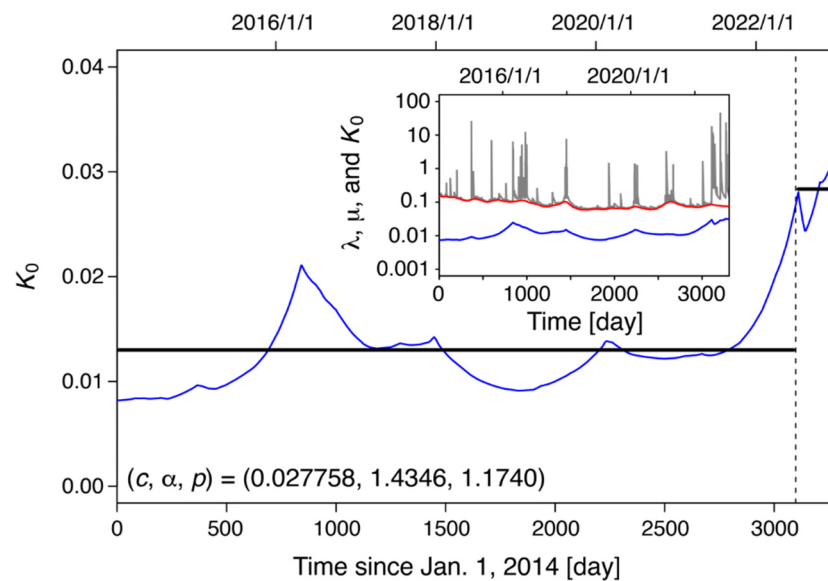


Figure 5. K_0 as a function of time. Earthquakes with $M \geq 2$ ($M_{th}=2$) for the period from 2014 to immediately before the $M7.7$ quake within a 50-km radius around its epicenter were used. Vertical dashed line indicates Jul. 9, 2022 ($T_c=2015$ days in Fig. 3). Horizontal lines indicate the mean values of K_0 for the periods before and after $T_c=2015$ days. Inset shows λ (grey), μ (red), and K_0 (blue) as a function of time, where c , α , and p are constants. For $M \geq 1.5$, see Figure S1.

We obtained the α , c , and p -values obtained for the standard (single) ETAS fitting to the earthquakes ($M \geq 2$) over the period from 2014 to immediately before the $M7.7$ quake in the region within a 50 km radius surrounding the future $M7.7$ epicenter. Then, the obtained α , c , and p -values were assumed to be applicable to the non-stationary ETAS model with $\mu(t)$, $K_0(t)$, and $\lambda(t)$. Namely, the α , c , and p -values were independent of t . Given the predefined $\alpha=1.43$, $c=0.028$, and $p=1.17$ for $M_{th}=2$ ($M \geq 2$), μ (red), K_0 (blue), and λ (grey) were computed for each earthquake (inset of Figure 5). Visual inspection shows that μ was nearly constant over time. However, K_0 was visually larger after mid-2022 than before it, although the timeseries of K_0 before mid-2022 showed one tall peak in 2016. Focusing on the time-dependent K_0 , we included, in Figure 5, the average (horizontal solid line) of K_0 -values for the periods before and after Jul. 9, 2022 ($T_c=2015$ days) (vertical dashed line). The average of K_0 -values after Jul. 9, 2022 was nearly equal to K_0 -values around the tall peak in 2016. The result shows that K_0 was larger after the start of seismic activation than before it, suggesting that clustering had an influence on months-long activation surrounding the $M7.7$ -quake nucleation region. The increase in K_0 is consistent with the emergence of clusters C1 and C2 [10] within 8 months prior to the $M7.7$ quake. The same analysis was conducted for $M \geq 1.5$ (Figure S1), supporting our result.

4.1.3. Slip Distribution of the $M7.7$ Quake and Preceding Seismicity

A cross-sectional view (Figure 6a) shows the slip distribution on segment 2 where the $M7.7$ quake initiated [2] and seismicity after the start of the activation (circles) (from Jul. 1, 2022 to immediately before the $M7.7$ quake). To create this cross-section, we used the AFAD catalog and retrieved $M \geq 2$ events within 7.5 km from the segment (width of 15 km). The retrieved events mostly consisted of events within cluster C2 [10]. An area of high-slip values of >1.5 m (red) was separated by about 10 km from the $M7.7$ hypocenter (star). This high-slip area overlaps with seismicity after the start of the activation (circles). A similar result was obtained (Figure 6b), using the catalog of Kwiatak

et al. [10], into which events during the period from Jan. 1, 2023 to immediately before the $M7.7$ quake were included. We considered $M \geq 0.5$ events, because M_c for the catalog was 0.5 [10]. We similarly investigated the catalog of Lomax [16]. The number of earthquakes ($M \geq 1.5$, from Jan. 1, 2023 to immediately before the $M7.7$ quake) was inadequate (Figure 6c), although the result is consistent with those in Figure 6a,b. Given that cluster C2 contributed to the display of low b -values ($b=0.6$ [10]), our result indicates that the zone of low b -values coincided with the location of a future high-slip area on segment 2. This is similar to the result obtained by Nanjo et al. [30], who compared the slip distribution of the 2011 $M9$ Tohoku earthquake in Japan and the distribution of areas with low b -values of seismicity since 2008 to immediately before the Tohoku earthquake. Those authors showed that the zones of extremely low b -values coincided remarkably with locations of an extremely large co-seismic slip.

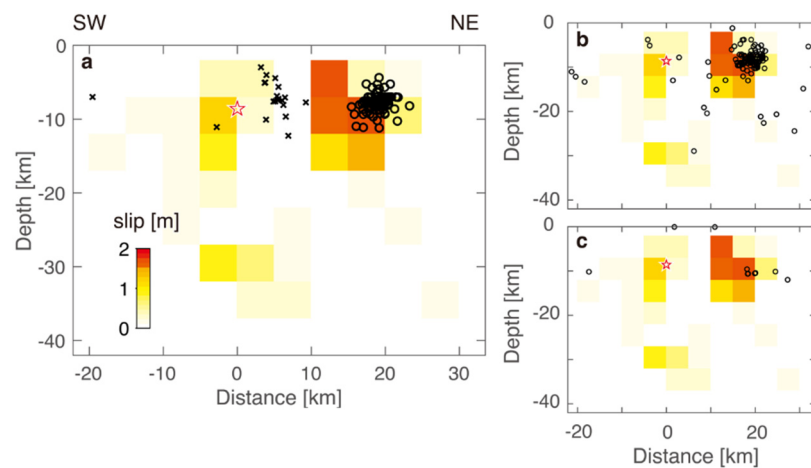


Figure 6. Slip distribution along the segment 2 from which the $M7.7$ quake initiated [2]. Star indicates the $M7.7$ hypocenter. (a) We used the AFAD catalog. Events ($M \geq 2$) within 7.5 km from this segment (width of 15 km) are shown by circles and crosses. Circles indicate events from Jul. 1, 2022 to immediately before the $M7.7$ quake. Crosses indicate the same as circles for events during Oct. 23, 2017 to Jan. 21, 2018 (2017.9-2018.1 decimal years). (b) Same as a, but we used the catalog of Kwiatek et al. [10]. Circles indicate events ($M \geq 0.5$) within 7.5 km from the segment from Jan. 1, 2023 to immediately before the $M7.7$ quake, where $M=0.5$ is the completeness magnitude according to Kwiatek et al. [10]. (c) Same as b but we used the catalog of Lomax [16]. Circles indicate events ($M \geq 1.5$) within 7.5 km from the segment from Jan. 1, 2023 to immediately before the $M7.7$ quake, where $M=1.5$ is the minimum magnitude for earthquakes recorded in the catalog of Lomax [16].

Also included in Figure 6a is the distribution of a swarm (crosses) in late 2017 to early 2018, shown as an upward convex around 340 days in ordinary time in Figure 4a or 40 in transformed time in Figure 4b. This swarm corresponds to cluster C7 [10]. The majority of this swarm overlaps with a low-slip area (white to light yellow). Cluster C7 displayed a high b -value ($b=0.9$ [10]). The observation between a high b -value and a low slip is also consistent with a previous study [30].

4.2. Post-Doublet-Quake Sequence

4.2.1. Seismicity Immediately After the Doublet Quakes

We calculated Coulomb stresses imparted by the doublet quakes and their relationship to seismicity within 5 days after the $M7.7$ quake (Figure 7a), where we used the USGS source models of the $M7.7$ and 7.5 quakes [2,3] and the AFAD earthquake catalog. In creating Figure 7a, the stresses were resolved on idealized faults oriented parallel to segment 1 (strike/dip/rake= $60^\circ/85^\circ/3^\circ$) of the $M7.7$ source [2] and, therefore, similar to the broad character of the EAFZ. We observed a lack of seismicity at the zone of increase in Coulomb stress beyond the north end of the $M7.7$ rupture, noting that the area, which lacked seismicity, closely matched the area of the $M6.8$ rupture (Figure 7b). To create this figure, the same Coulomb stress calculation as was used in Figure 7a was conducted, but

we used seismicity within 1 day after the 2020 $M6.8$ earthquake, which outlined the 2020 $M6.8$ -quake source. Stress in the area beyond the north end of the $M7.7$ rupture was released by the 2020 $M6.8$ quake so that the increase in stress imparted by the doublet quakes was insufficient to induce the following events in this area. This is consistent with the result obtained by Toda and Stein [5], who showed that the 2020 $M6.8$ quake locally dropped the stress by ~ 10 bars, and the $M7.7$ quake then increased the stress there by 1-2 bars, resulting in a hole in seismicity after the $M7.7$ quake.

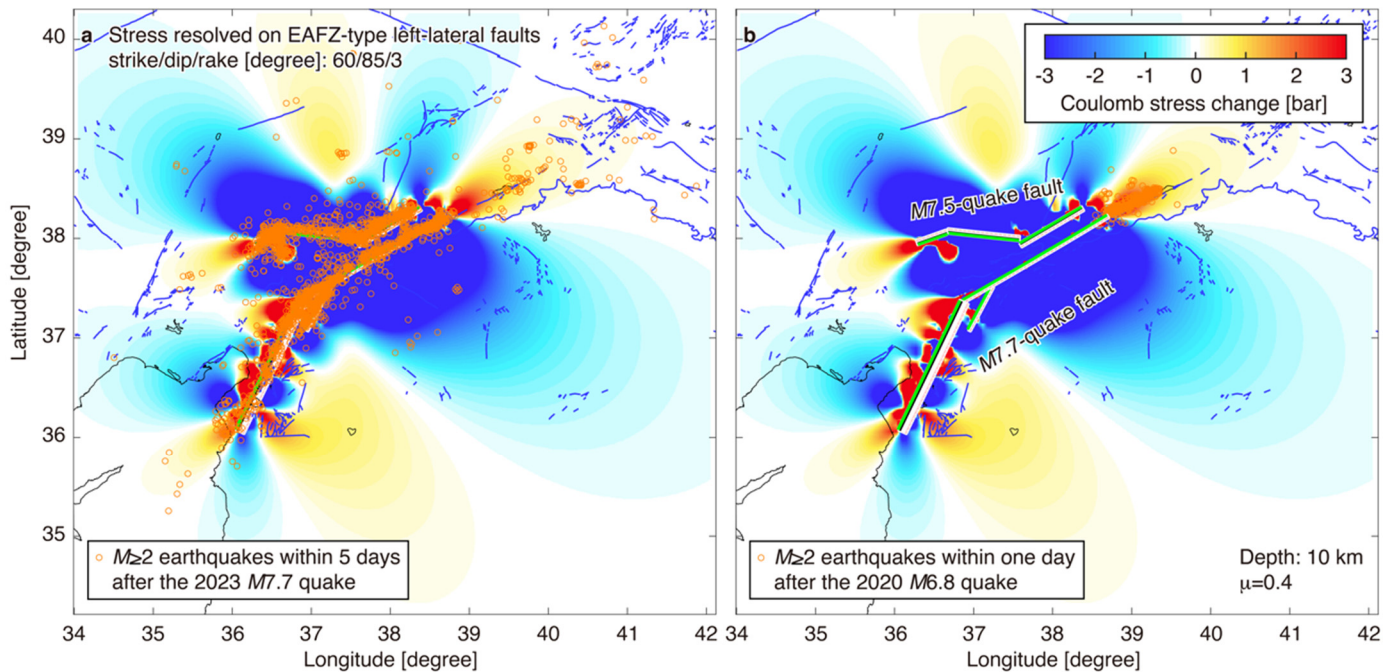


Figure 7. Coulomb stress changes as a result of the 2023 $M7.7$ and 7.5 quakes. (a) Changes in stress imparted to surrounding faults under the assumption that all faults are parallel to the main rupture (segment 1) of the $M7.7$ earthquakes. Circles indicate events ($M \geq 2$, and depths shallower than 40 km) within 5 days after the $M7.7$ quake occurred. Green lines indicate the $M7.7$ and 7.5-quake fault models [2,3]. Blue lines indicate active faults. (b) Same as a for events within 1 day after the 2020 $M6.8$ quake occurred.

4.2.2. Seismicity Until the $M6.4$ Quake

The largest event ($M6.4$) after the doublet quakes occurred on Feb. 20, 2023 in an area around the south end of the $M7.7$ rupture. In creating Figure 8a, we conducted the same stress calculation as that in Figure 7a, but resolved stresses on faults oriented parallel to the NP1 (strike/dip/rake= $225^\circ/53^\circ/-27^\circ$) of the $M6.4$ source [13]. The fault that ruptured during the $M6.4$ quake was promoted toward failure. The same resolution was conducted for the NP2 (strike/dip/rake= $333^\circ/69^\circ/-139^\circ$), and a similar result was obtained (Figure 8b). Över et al. [11] obtained a result consistent with Figure 8a.

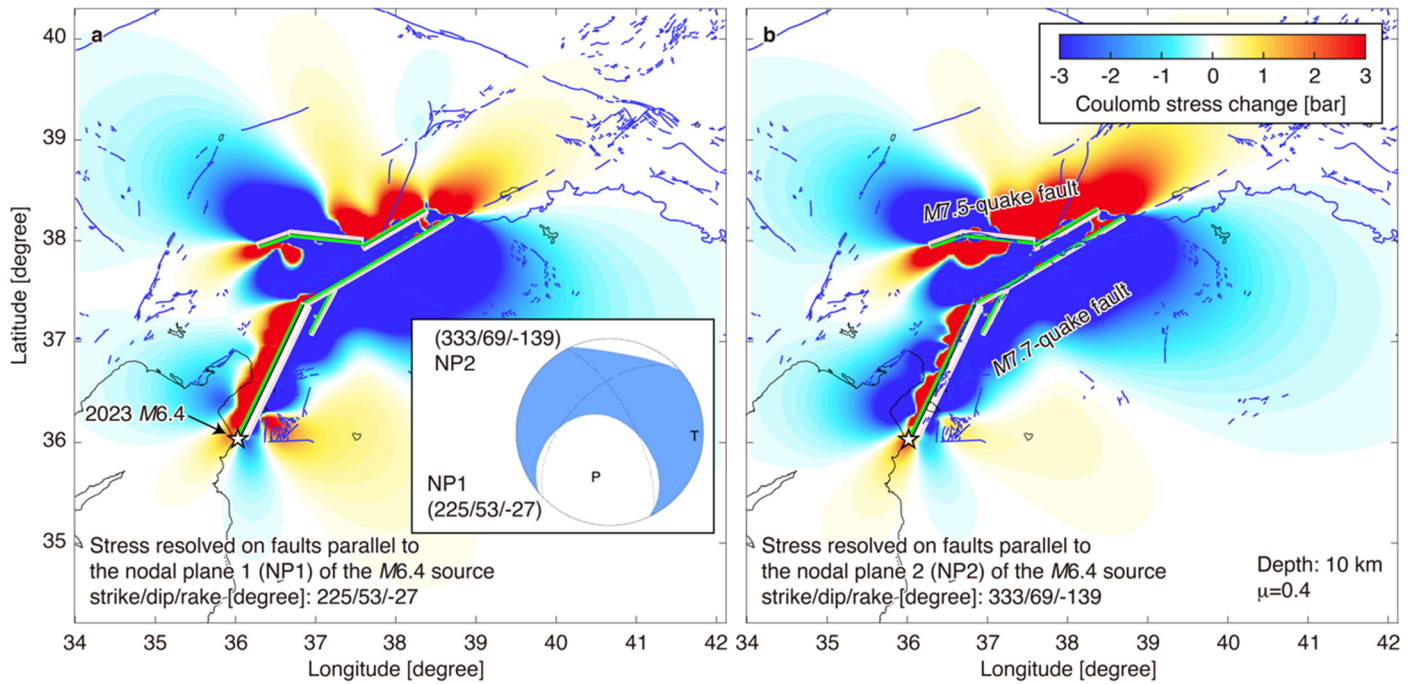


Figure 8. Same as Figure 7a for stresses resolved on faults parallel to the NP1 of the Feb. 20, 2023 M6.4 source [13] in **a** and the NP2 in **b**. Star indicates the epicenter of the M6.4 quake. Inset shows the beach ball indicating the focal mechanism of the M6.4 quake [13]. The NP1 and NP2 are shown. The P and T axes are also plotted.

A map view based on data from the AFAD catalog for the period from Feb. 12, 2023 to immediately before the M6.4 quake (Figure 9a) shows that the eventual epicenter fell in a region of low b -values (red), where the period until Feb. 11, 2023 was not considered to remove the effect of the main aftershock sequence, revealing strong temporal variability in b . To create this map, we computed b -values [21,22] for events falling in a cylindrical volume, with height=30 km and sampling radius $r=20$ km, centered at each node on a $0.05^\circ \times 0.05^\circ$ grid, and plotted a b -value at the corresponding node. According to a previous study [48], r was searched by mapping b -values with a range of $r=10$ -30 km to find optimal r (Figures S2 and S3). A nearly identical pattern of b -values, when sampled with $r=15$ -20 km, was observed. Using $r=10$ km did not reveal details because it only reduced coverage. Sampling with $r \geq 25$ km resulted in smoothed b -values. For $r=30$ km, the low b -value zone lost its crispness and moved toward the outside. This is because the small volumes containing information about the low b -values were located at the edge of seismically active regions. At the locus of the b -value anomaly, the sample became a mixture of different distributions when r was increased. As a result, the anomaly was visually reduced. Thus, the optimal r was in the range of 15-20 km. In Figure 9, $r=20$ km was used, but using $r=15$ km, which slightly reduced coverage, did not change the conclusion. The corresponding M_c maps are given in Figure S2, where M_c was simultaneously calculated when calculating the corresponding b -value [22]. A similar feature was observed in Figure 9b by using the catalog of Lomax [16], where the mapping procedure was the same as that used for Figure 9a (see Figures S4 and S5).

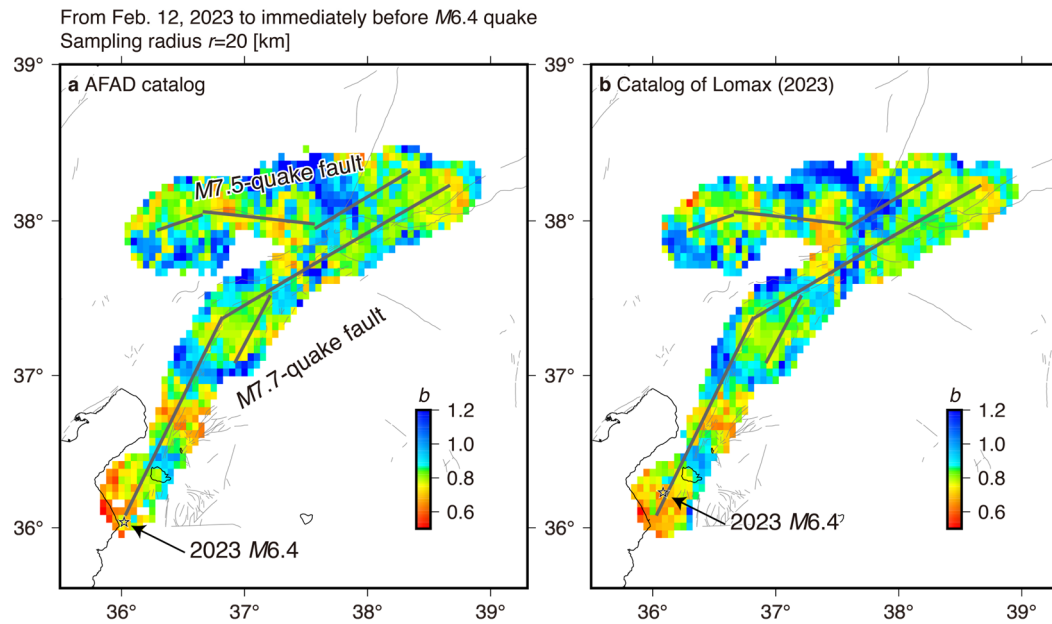


Figure 9. Map views of b -values before the Feb. 20, 2023 $M6.4$ quake (star), using the AFAD catalog in **a** and the catalog of Lomax [16] in **b**. In **a** and **b**, earthquakes during the period from Feb. 12 to immediately before the $M6.4$ quake were used. The $M6.4$ -quake epicenter (star) in **a** is different from that in **b**, because the epicenter of the $M6.4$ quake in the AFAD catalog is different from that in the catalog of Lomax [16]. Thick grey segments show fault models of the $M7.7$ and 7.5 quakes [2,3]. Thin grey lines indicate active faults.

4.2.3. Seismicity Until the $M5.9$ Quake

The second largest event ($M5.9$) after the doublet quakes occurred on Oct. 16, 2024 in an area around the north end of the $M7.7$ rupture. The same stress calculation as in Figure 7a was conducted, but different receiver faults [14] were used. Namely, we used two NPs of the $M5.9$ source: strike/dip/rake= $244^\circ/43^\circ/-8^\circ$ in Figure 10a and $340^\circ/84^\circ/-133^\circ$ in Figure S6b. The result shows that the fault that ruptured during the $M5.9$ quake was promoted toward failure by the double quakes, irrespective of the plane that was used (Figures 10a and S6b). We conducted the same stress calculation as in Figures 10a and S6b, except that the $M6.8$ -quake fault [4] was added into source faults. A similar feature was observed (Figures 10b and S6a).

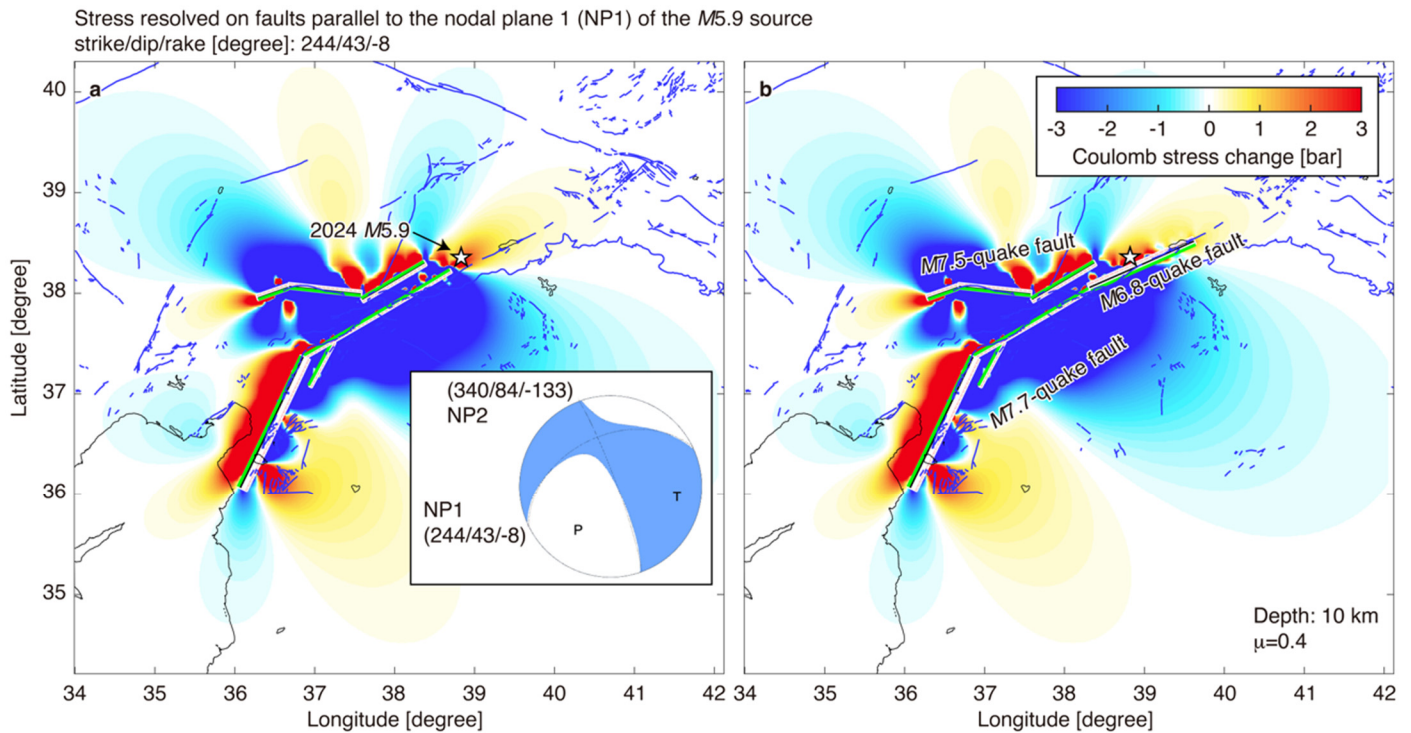


Figure 10. Coulomb stress changes resolved on faults parallel to the NP1 of the Oct. 16, 2024 M5.9 source [14]. (a) Changes in stress imparted by the M7.7 and 7.5 quakes in 2023. Star indicates the epicenter of the M5.9 quake. Inset shows the beach ball indicating the focal mechanism of the M5.9 quake [14]. (b) Changes in stress imparted by the M6.8 quake in 2020 and the M7.7 and 7.5 quakes in 2023. For the NP2, see Figure S6.

A map view based on use of the AFAD catalog for the period from Feb. 21, 2023 to Oct. 15, 2024 shows a zone of relatively low b -values (yellow to green) around the future epicenter (Figure 11a). The mapping procedure was the same as that in Figure 9a. The optimal r was in the range of 15-20 km (Figures S7 and S8). Similar to Figure 9a, we decided to use $r=20$ km in Figure 11a. This feature generally appears when using the catalog of Lomax [16] (Figures 11b, S9, and S10).

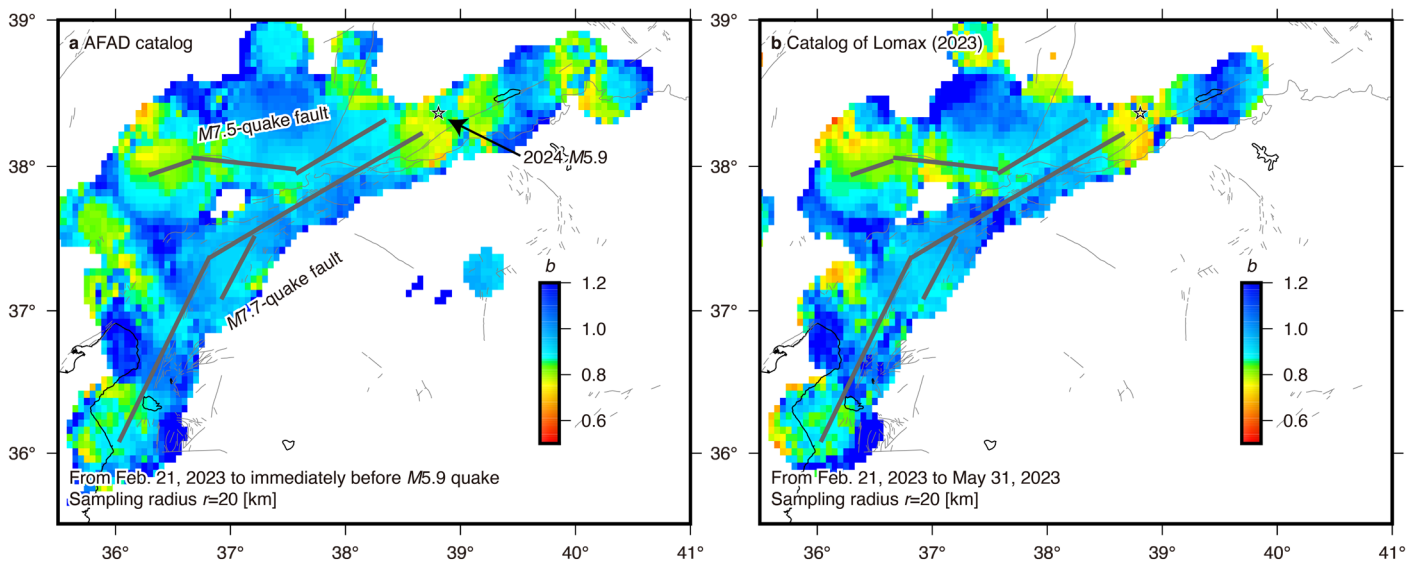


Figure 11. Map views of b -values before the Oct. 16, 2024 M5.9 quake (star), using the AFAD catalog in **a** and the catalog of Lomax [16] in **b**. Grey segments show fault models of the M7.7 and 7.5 quakes [2,3].

5. Discussion

As was pointed out in the Introduction, we discussed a comparison of the duration of the post-doublet-quake sequence between our study and a previous study [5] to provide information that might possibly be used when evaluating a time-dependent seismic hazard along the NAFZ. As the basis of this comparison, we first confirmed that the overall seismicity after the doublet quakes around the causative faults decayed with time (black curve in Figure 12a), where earthquakes of $M \geq 3$ in the AFAD catalog for the period from the $M7.7$ quake to Oct. 16, 2024 in the study region shown in Figure 11 were used. Visual inspection (Figure 12a) shows that the standard (single) ETAS model (red curve) fits the data after the $M7.7$ quake well, suggesting no pronounced activation and quiescence. Similar results were obtained for $M \geq 4$ (Figure S11). The results were not induced by catalog selection bias, because similar results were observed when using the catalog of Lomax [16] (Figures 12b and S12). The well-fitted results of the standard (single) ETAS model to the data (Figures 12, S11, and S12) allowed us to assume that use of the OU relation is enough to capture an essential aspect of seismicity decay following the doublet quakes and to estimate the expected duration of the post-doublet-quake sequence, as described below.

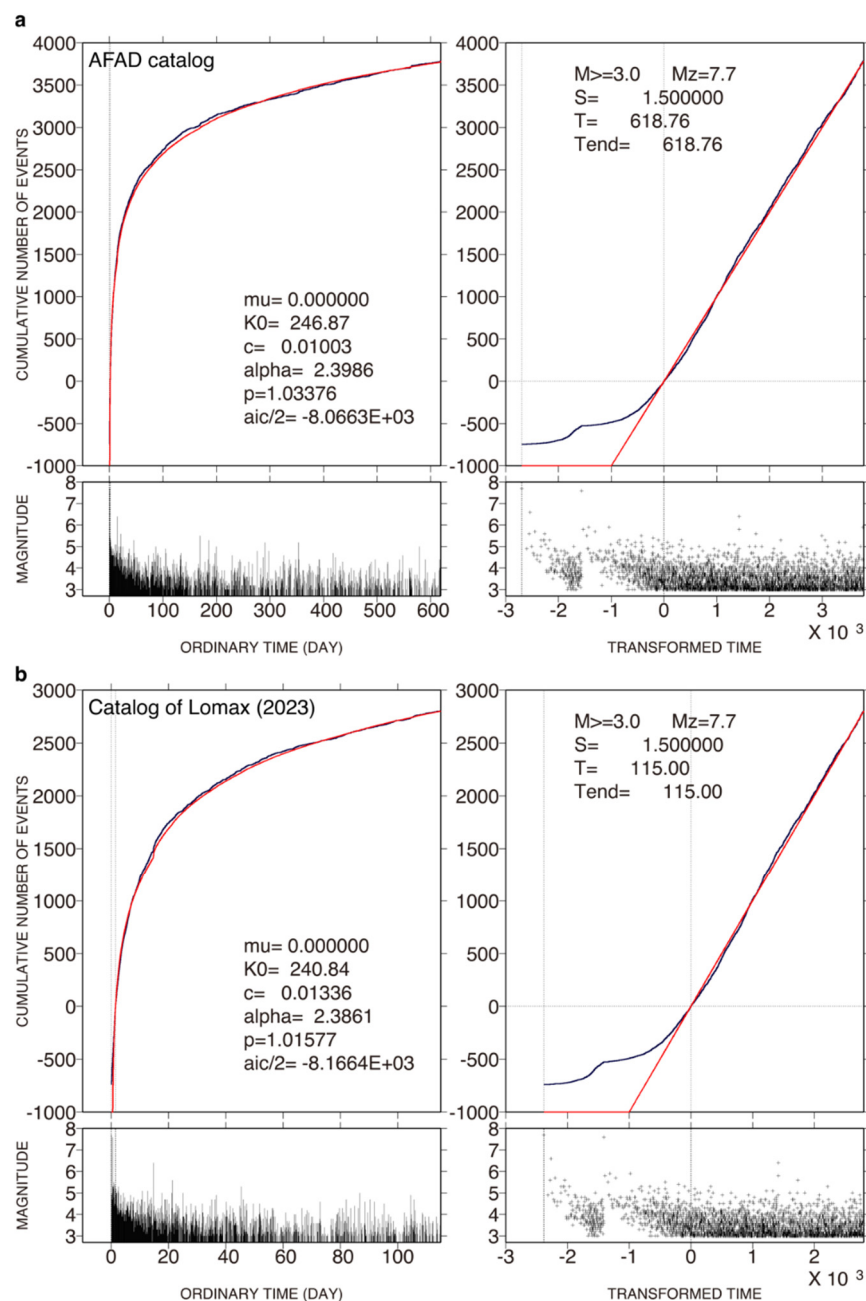


Figure 12. ETAS fitting to earthquakes after the $M7.7$ quake. (a) Cumulative function of $M \geq 3.0$ earthquakes in the AFAD catalog is plotted against ordinary time (left panel) and transformed time (right panel), showing the ETAS fitting in the target interval from 1.5 days after the $M7.7$ quake to Oct. 16, 2024, where precursor interval is from the moment of the $M7.7$ quake to 1.5 days after the $M7.7$ quake. The smaller panel below each larger panel indicates an M -time diagram. (b) Same as a for using the catalog of Lomax [16].

As was done by Toda and Stein [5], we correlated the earthquake sequence with the OU relation, where we used events of $M \geq 3$ (green circles in Figure 13) in the AFAD catalog (from immediately after the $M7.7$ quake to Oct. 16, 2024 in the region considered for Figure 11). A similar correlation was obtained by using the catalog of Lomax [16] (green crosses). We used the ordinary occurrence rate of 0.3 $M \geq 3$ earthquakes per day (horizontal green line), based on the number of $M \geq 3$ earthquakes in the AFAD catalog during the period from 2014 to immediately before the 2020 $M6.8$ quake in the region considered for Figure 11. The intersection between the horizontal green line and the green curve shows an expected duration of about $1-2 \times 10^3$ days. Similar expected durations were obtained for $M \geq 2$ (red) and $M \geq 4$ (blue) (Figure 13).

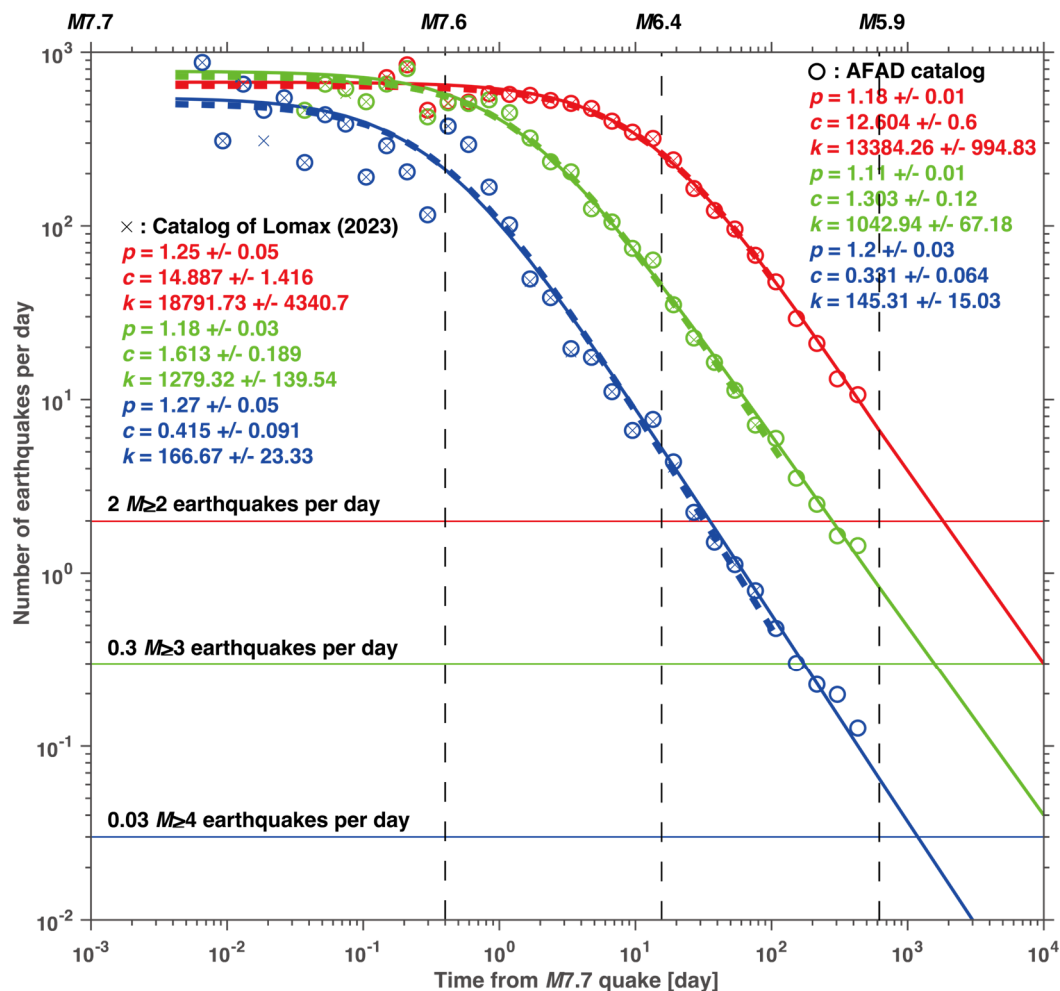


Figure 13. Number of earthquakes per day, λ_{OU} , as a function of time t since the $M7.7$ quake is correlated with the OU relation. Earthquakes of $M \geq 2$ (red), $M \geq 3$ (green), and $M \geq 4$ (blue) in the AFAD catalog (circles and solid curves) were used. The parameter values of the OU relation are given at the upper right corner. The standard deviation of the respective parameters of the bootstrap samples was used to define the corresponding error bars. Vertical lines indicate the moments of the $M7.5$, 6.4 , and 5.9 quakes. Horizontal line indicates the rate of earthquakes of $M \geq 2$ (red), $M \geq 3$ (green), and $M \geq 4$ (blue) obtained for the period from 2014 to immediately before the 2020 $M6.8$ quake. Also included for comparison is the correlation with the OU relation for using the catalog of Lomax [16] (crosses and dashed curves).

Our expected duration was longer than that (1-2.5 years) obtained by Toda and Stein [5]. We assumed a more stable fitting of the OU relation to data in the present study than in the previous study. This is because Toda and Stein fitted the OU relation to earthquakes during the period of about 100 days since the $M7.7$ quake while we completed this process for a period of 618 days since the $M7.7$ quake, i.e., the period (about 100 days) considered by Toda and Stein was shorter than the period (618 days) we considered. Similar to Toda and Stein [5], we considered the earthquake sequence of $M \geq 4.5$ to obtain the estimated duration (Figure S13). This sequence is correlated with the OU relation. An ordinary occurrence rate of 0.006 $M \geq 4.5$ earthquakes per day was used. The expected duration was about $1-2 \times 10^3$ days. This is similar to the expected durations obtained for $M \geq 2, 3$, and 4, and longer than that in a previous study [5].

During the 20th century, much of the northern section of the EAFZ ruptured, as described in the Introduction. Starting with the 2020 $M6.8$ -quake sequence, much of the southern section ruptured (Figure 1). There is no doubt that the $M7.7$ quake was not the almighty earthquake [49], which would rupture an entire plate boundary at once and leave no stress that could produce any other kind of earthquake. Regional and global earthquake magnitude frequency distributions obey a GR relation (e.g., [29–31,48,50]), but it is unclear if individual fault zones do. Namely, earthquake magnitude-frequency on fault zones is suggested to be distributed in a GR relation or characteristic. Parsons et al. [51] used data from California, USA and found that individual fault zones have characteristic magnitude distributions, with a greater number of large earthquakes relative to small earthquakes than expected from a GR trend (e.g., [52]).

We conducted a simple test to examine whether seismicity along the EAFZ obeys a GR relation or not (Figure 14), where a lower magnitude threshold ($M=5.5$) was set to ensure the homogeneity of earthquake recording since 1965. To create Figure 14, we used the same catalog as that used in Figure 1 (see the Data section). Analysis of the b -value [21,22] shows that the $M7.7$ quake (star) followed the GR trend with $b \sim 1$ (Figure 14b), indicating that the EAFZ does not have a characteristic magnitude distribution, where we used earthquakes during the period from Jan. 1, 1965 to Feb. 25, 2023. As a reference, we conducted a similar analysis, using data before the $M7.7$ quake. Figure 14a, which indicates the GR distribution with $b \sim 1$, shows that the $M7.7$ quake (star) deviates from this distribution, where the $M7.7$ quake was not included in the GR fitting. A comparison between these figures (Figure 14a,b) indicates that the $M7.7$ quake and the following events, including the $M7.5$ quake, affected the whole magnitude range, such that the $M7.7$ quake continued to follow the GR trend (Figure 14b). A similar feature was observed for the effect of the 2004 Sumatran megaquake, in Indonesia, on a global catalog [50]. Our result supports the observation that the $M7.7$ quake was not an outlier (neither an almighty earthquake nor a characteristic earthquake), but was instead harmonized with small earthquakes along the EAFZ. If an almighty earthquake or a characteristic earthquake of the EAFZ existed, it would be much larger than the $M7.7$ quake.

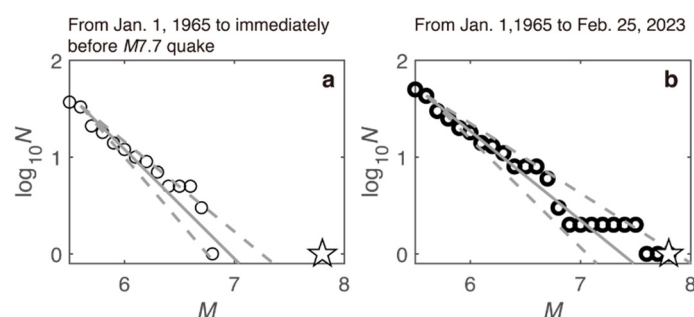


Figure 14. Cumulative number of earthquakes as a function of M . (a) Earthquakes during the period from Jan. 1 1965 to immediately before the $M7.7$ quake (the top outside of axes) in the rectangle shown in Figure 1a were used. Solid line represents the GR relation with $b=1.13$ and $a=7.86$. The GR relation, taking the upper and lower bounds (standard deviation) of b -values ($b=1.33$ and 0.93), is shown by dashed lines, where the standard deviation of the b -values of the bootstrap samples was used to define these bounds. Also included for comparison is the $M7.7$ quake (star), where this quake was not included in the data to which the GR relation was

fitted. (b) Earthquakes during the period given at the top outside of axes in the rectangle shown in Figure 1a were used. The GR relation with $b=0.92\pm0.20$ and $a=6.80$ is shown by a solid line and dashed lines, respectively. The $M7.7$ quake (star) was included in the data to which the GR relation was fitted.

The feature that the $M7.7$ quake continued to follow the GR trend (Figure 14b) implies that underlying mechanism of earthquake occurrence did not differ from small events to large events. A phenomenon served by the mechanism we focused on is earthquake clustering, namely seismicity prior and subsequent to the $M7.7$ quake. Given that this quake and the $M7.5$ quake that occurred about nine hours later were defined as the doublet quakes, this paper reported the characteristics of seismicity before and after the doublet quakes. The possibility to analyze the interaction between the doublet quakes was out of scope in the present study because several studies [5–9] performed in-depth analyses of it.

There are three features of the pre-doublet-quake sequence:

- Seismicity transients began in mid-2022 within 50 km of the future $M7.7$ epicenter. We revealed that the occurrence rate after mid-2022 was significantly larger than that before it, showing seismic activation. Small b -values were observed after the start of activation. The transients reported previously [10,11] were confirmed by our study, which applied the ETAS model and the Bayesian b -value model to events in two different earthquake catalogs.
- Seismicity within 50 km of the future $M7.7$ epicenter decomposed into two types of activity: background and clustering. The parameter representing background activity was almost constant over time while that representing clustering activity was smaller before the start of activation than after it. Seismic activation is interpreted as the effect of clustering activity. This was attributed to the emergence of two clusters near the future $M7.7$ epicenter [10].
- A high-slip area on the segment (referred to as segment 2 in this study) from which the $M7.7$ rupture started, overlaps with seismicity after the start of activation. This seismicity mostly consisted of events of the cluster displaying low b -values. A similar result was observed for the 2011 Tohoku megaquake [30], where a correlation between areas of low b -values and areas of large co-seismic displacement was shown. A cluster of high b -values that emerged in 2017-2018 overlapped with a low-slip area on the same segment.

There are three features pertaining to seismicity after the doublet quakes:

- Seismicity following the 2020 $M6.8$ quake suggests that the south end of the $M6.8$ rupture was close to the north end of the $M7.7$ rupture. There was a lack of post- $M7.5$ -quake seismicity at the zone of increase in Coulomb stress imparted by the doublet quakes beyond the north end of the $M7.7$ rupture, noting that this area, which lacked seismicity, closely matched the area of the 2020 $M6.8$ rupture. Our result is consistent with a previous finding [5].
- Locations of the two $M6$ -class quakes around the north and south ends of the $M7.7$ -quake rupture were in relatively high-stress regions compared with the surrounding ones, as implied by the b -value and Coulomb-stress analyses. The region around the hypocenters of the $M6$ -class quakes became closer to failure by the doublet quakes. A similar result was obtained when adding the 2020 $M6.8$ fault to source faults of Coulomb stress changes.
- The decay of seismic activity with time after the $M7.7$ quake around the causative faults was well modeled by the standard (single) ETAS model, indicating no pronounced activation or quiescence. This decay also followed the OU relation. Our estimation of the duration of the post-doublet-quake sequence was $1\text{--}2\times10^3$ days (2.7–5.5 years), a longer duration than that proposed by an earlier study [5]. The difference between the present study and the previous study emerged from the fact that the former used events within 618 days since the $M7.7$ quake while the latter used events within about 100 days.

Supplementary Materials: The following supporting information can be downloaded at the website of this paper posted on Preprints.org, Figure S1: λ , μ , and K_0 as a function of time for $M_{th}=2.0$ and 1.5; Figure S2: Map views of b -values before the Feb. 20, 2023 $M6.4$ quake; Figure S3: Same as Figure S2 for M_c ; Figure S4: Same as Figure S2 for using the catalog of Lomax [16]; Figure S5: Same as Figure S4

for M_c ; Figure S6: Coulomb stress changes; Figure S7: Same as Figure S2 for using earthquakes during the period from Feb. 21 to immediately before the $M_{5.9}$ quake; Figure S8: Same as Figure S7 for M_c ; Figure S9: Same as Figure S7 for using the catalog of Lomax [16]; Figure S10: Same as Figure S9 for M_c ; Figure S11: Same as Figure 12a for $M \geq 4$; Figure S12: Same as Figure 12b for $M \geq 4$; Figure S13: Same as Figure 13 for $M \geq 4.5$.

Author Contributions: Conceptualization, K.Z.N., J.I., T.H., T.N., and K.O.; methodology, K.Z.N. and T.K.; software, K.Z.N. and T.K.; validation, K.Z.N.; formal analysis, K.Z.N. and T.K.; investigation, K.Z.N. and T.K.; resources, K.Z.N.; data curation, K.Z.N.; writing—original draft preparation, K.Z.N.; writing—review and editing, K.Z.N., T.K., J.I., T.H., T.N., and K.O.; visualization, K.Z.N. and T.K.; supervision, K.Z.N.; project administration, K.Z.N.; funding acquisition, K.Z.N., T.K., J.I., T.H., and T.N. All authors have read and agreed to the published version of the manuscript.

Funding: This study was partially supported by the Ministry of Education, Culture, Sports, Science and Technology (MEXT) of Japan, under The Second Earthquake and Volcano Hazards Observation and Research Program (Earthquake and Volcano Hazard Reduction Research) (K.Z.N., T.K., J.I., T.N.) and under STAR-E (Seismology TowArD Research innovation with data of Earthquake) Program Grant Number JPJ010217 (K.Z.N., T.K.), and Collaboration Research Program of IDEAS, Chubu University Grant Number IDEAS202417 (J.I., T.N., K.Z.N.).

Data Availability Statement: The datasets used in the current study are available from the corresponding author upon reasonable request. The AFAD earthquake catalog was obtained from <https://deprem.afad.gov.tr/event-catalog>. The ANSS earthquake catalog was obtained from <https://earthquake.usgs.gov/data/comcat/>. The ISC-GEM earthquake catalog was obtained from <https://doi.org/10.31905/d808b825>. The earthquake catalog produced by Kwiatak et al. [10] is available as a part of the Supplementary Information of that study. The earthquake catalog produced by Lomax [16] is available at <https://zenodo.org/records/8089273>. The fault models of the 2020 $M_{6.8}$ quake, the 2023 $M_{7.7}$ quake, and the 2023 $M_{7.6}$ quake, which were used in this study, are based on previous work [2–4] (<https://earthquake.usgs.gov/earthquakes/eventpage/us60007ewc/executive>, <https://earthquake.usgs.gov/earthquakes/eventpage/us6000jllz/executive>, <https://earthquake.usgs.gov/earthquakes/eventpage/us6000jlqa/executive>). Moment tensor product of the 2023 $M_{6.4}$ and 2024 $M_{5.9}$ earthquakes [13,14] is available at <https://earthquake.usgs.gov/earthquakes/eventpage/us6000jqcn/executive> and <https://earthquake.usgs.gov/earthquakes/eventpage/us6000nyzk/executive>. The time dependence of b shown in Figure 3b of Kwiatak et al. [10] was used to create Figure 2. Active fault data provided by Emre et al. [53] were used. The seismicity analysis software package ZMAP [21], used for computing b -values [22] in Figures 9, 11, 14, S2-S5, and S7-S10, and for computing p -values in Figures 13 and S13, was obtained from <http://www.seismo.ethz.ch/en/research-and-teaching/products-software/software/ZMAP>. The program package XETAS [20], used for Figures 3, 4, 12, S11, and S12, was obtained from <http://evrrss.eri.u-tokyo.ac.jp/software/xetas/index.html>. The graphic-rich deformation and stress-change software Coulomb [33,34], used for Figures 7, 8, 10, and S6, is available for download at <https://earthquake.usgs.gov/research/software/coulomb/>. The Generic Mapping Tools [54], used for Figures 1, 9, 11, S2-S5, and S7-S10, are an open-source collection (<https://www.generic-mapping-tools.org>).

Acknowledgments: We thank S. Toda and Y. Yamamoto for discussion.

Conflicts of Interest: The authors declare no conflicts of interest.

Abbreviations

The following abbreviations are used in this manuscript:

AFAD	Disaster and Emergency Management Authority
AIC	Akaike Information Criterion
EAfZ	East Anatolian fault zone
ETAS	Epidemic-Type Aftershock Sequence
GR	Gutenberg-Richter

NAFZ	North Anatolian fault zone
NP	nodal plane
OU	Omori-Utsu
USGS	United States Geological Survey

References

1. USGS The 2023 Kahramanmaraş, Turkey, Earthquake Sequence. **2024**. <https://earthquake.usgs.gov/storymap/index-turkey2023.html> (Accessed on Feb. 15, 2025).
2. USGS M7.8-Pazarcik earthquake, Kahramanmaraş earthquake sequence. **2023**. <https://earthquake.usgs.gov/earthquakes/eventpage/us6000jllz/executive> (Accessed on Feb. 15, 2025).
3. USGS M7.5-Elbistan earthquake, Kahramanmaraş earthquake sequence. **2023**. <https://earthquake.usgs.gov/earthquakes/eventpage/us6000jlqa/executive> (Accessed on Feb. 15, 2025).
4. USGS M6.7-13 km N of Doğanyol, Turkey. **2020**. <https://earthquake.usgs.gov/earthquakes/eventpage/us60007ewc/executive> (Accessed on Feb. 15, 2025).
5. Toda, S.; Stein, R. The role of stress transfer in rupture nucleation and inhibition in the 2023 Kahramanmaraş, Türkiye, sequence, and a one-year earthquake forecast. *Seismological Research Letters* **2024**, *95*(2A), 596-606. <https://doi.org/10.1785/0220230252>.
6. Chen, J.; Liu, C.; Dal Zilio, L.; Cao, J.; Wang, H.; Yang, G.; Göğüş O.H.; Zhang, H.; Shi, Y. Decoding Stress Patterns of the 2023 Türkiye-Syria Earthquake Doublet. *Journal of Geophysical Research* **2024**, *129*(10), e2024JB029213. <https://doi.org/10.1029/2024JB029213>.
7. Toda, S.; Stein, R.S.; Özbakir, A.D.; Gonzalez-Huizar, H.; Sevilgen, V.; Lotto, G.; Sevilgen, S. Stress change calculations provide clues to aftershocks in 2023 Türkiye earthquakes. *Temblor* **2023**. <http://doi.org/10.32858/temblor.295>.
8. Kobayashi, T.; Munekane, H.; Kuwahara, M.; Furui, H. Insights on the 2023 Kahramanmaraş Earthquake, Turkey, from InSAR: fault locations, rupture styles and induced deformation. *Geophysical Journal International* **2024**, *236*(2), 1068-1088. <https://doi.org/10.1093/gji/ggad464>.
9. Ren, C. et al. Supershear triggering and cascading fault ruptures of the 2023 Kahramanmaraş, Türkiye, earthquake doublet. *Science* **2024**, *383*(6680), 305-311. <https://doi.org/10.1126/science.adi151>.
10. Kwiatek, G.; Martínez-Garzón, P.; Becker, D.; Dresen, G.; Cotton, F.; Beroza, G.C.; Acael, D.; Ergintav, S.; Bohnhoff, M. Months-long seismicity transients preceding the 2023 Mw 7.8 Kahramanmaraş earthquake, Türkiye. *Nature Communications* **2023**, *14*, 7534. <https://doi.org/10.1038/s41467-023-42419-8>.
11. Över, S.; Demirci, A.; Özden, S. Tectonic implications of the February 2023 Earthquakes (Mw7.7, 7.6 and 6.3) in south-eastern Türkiye. *Tectonophysics* **2023**, *866*, 230058. <https://doi.org/10.1016/j.tecto.2023.230058>.
12. Gutenberg, B.; Richter, C.F. Frequency of earthquakes in California. *Bulletin of the Seismological Society of America* **1944**, *34*(4), 185-188. <https://doi.org/10.1785/BSSA0340040185>.
13. USGS M6.3-2 km NNW of Uzunbağ, Turkey. **2023**. <https://earthquake.usgs.gov/earthquakes/eventpage/us6000jqcn/executive> (Accessed on Feb. 15, 2025).
14. USGS M6.0-19 km W of Doğanyol, Turkey. **2024**. <https://earthquake.usgs.gov/earthquakes/eventpage/us6000nyzk/executive> (Accessed on Feb. 15, 2025).
15. Utsu, T. A statistical study on the occurrence of aftershocks. *Geophysical Magazine* **1961**, *30*(4), 521-605.
16. Lomax, A. Precise, NLL-SSST-coherence hypocenter catalog for the 2023 Mw 7.8 and Mw 7.6 SE Turkey earthquake sequence. **2023**. <https://zenodo.org/records/8089273> (Accessed on Feb. 15, 2025).
17. Ogata, Y., Statistical models for earthquake occurrences and residual analysis for point processes. *Journal of the American Statistical Association* **1988**, *83*, 9-27. <https://doi.org/10.2307/2288914>.
18. Dieterich, J. 1994. A constitutive law for rate of earthquake production and its application to earthquake clustering. *Journal of Geophysical Research* **1994**, *99*(B2), 2601-2618. <https://doi.org/10.1029/93JB02581>.
19. Akaike, H. A new look at the statistical model identification. *IEEE Transactions on Automatic Control* **1974**, *19*(6), 716-723. <https://doi.org/10.1109/TAC.1974.1100705>.
20. Ogata, Y.; Tsuruoka, H. Statistical monitoring of aftershock sequences: a case study of the 2015 Mw7.8 Gorkha, Nepal, earthquake. *Earth, Planets and Space* **2016**, *68*, 44. <https://doi.org/10.1186/s40623-016-0410-8>.

21. Wiemer, S. A software package to analyze seismicity: ZMAP. *Seismological Research Letters* **2012**, 72(3), 373-382. <https://doi.org/10.1785/gssrl.72.3.373>.
22. Woessner, J.; Wiemer, S. Assessing the quality of earthquake catalogues: estimating the magnitude of completeness and its uncertainty. *Bulletin of the Seismological Society of America* **2005**, 95, 684-698. <https://doi.org/10.1785/0120040007>.
23. Nanjo, K.Z.; Yoshida, A. A b map implying the first eastern rupture of the Nankai Trough earthquakes. *Nature Communications* **2018**, 9, 1117. <https://doi.org/10.1038/s41467-018-03514-3>.
24. Kumazawa, T.; Ogata, Y.; Tsuruoka, H. Characteristics of seismic activity before and after the 2018 M6.7 Hokkaido Eastern Iwate earthquake. *Earth, Planets and Space* **2019**, 71, 130. <https://doi.org/10.1186/s40623-019-1102-y>.
25. Nanjo, K.Z. Were changes in stress state responsible for the 2019 Ridgecrest, California, earthquakes? *Nature Communications* **2020**, 11, 3082. <https://doi.org/10.1038/s41467-020-16867-5>.
26. Scholz, C.H. The frequency-magnitude relation of microfracturing in rock and its relation to earthquakes. *Bulletin of the Seismological Society of America* **1968**, 58(1), 399-415. <https://doi.org/10.1785/BSSA0580010399>.
27. Lei, X. How do asperities fracture? An experimental study of unbroken asperities. *Earth Planetary Science Letters* **2003**, 213(3-4), 347-359. [https://doi.org/10.1016/S0012-821X\(03\)00328-5](https://doi.org/10.1016/S0012-821X(03)00328-5).
28. Goebel, T.H.W.; Schorlemmer, D.; Becker, T.W.; Dresen, G.; Sammis, C.G. Acoustic emissions document stress changes over many seismic cycles in stick-slip experiments. *Geophysical Research Letters* **2013**, 40, 2049-2054. <https://doi.org/10.1002/grl.50507>.
29. Tormann, T.; Enescu, B.; Woessner, J.; Wiemer, S. Randomness of megathrust earthquakes implied by rapid stress recovery after the Japan earthquake. *Nature Geoscience* **2015**, 8, 152-158. <https://doi.org/10.1038/ngeo2343>.
30. Nanjo K.Z., Hirata, N.; Obara, K.; Kasahara, K. Decade-scale decrease in b value prior to the M9-class 2011 Tohoku and 2004 Sumatra quakes. *Geophysical Research Letters* **2012**, 39(20), L20304. <https://doi.org/10.1029/2012GL052997>.
31. Schurr, B. et al. Gradual unlocking of plate boundary controlled initiation of the 2014 Iquique earthquake. *Nature* **2014**, 512, 299-302. <https://doi.org/10.1038/nature13681>.
32. Ito, R.; Kaneko, Y. Physical mechanism for a temporal decrease of the Gutenberg-Richter b -value prior to a large earthquake. *Journal of Geophysical Research* **2023**, 128(12), e2023JB027413. <https://doi.org/10.1029/2023JB027413>.
33. Lin, J.; Stein, R.S. Stress triggering in thrust and subduction earthquakes, and stress interaction between the southern San Andreas and nearby thrust and strike-slip faults. *Journal of Geophysical Research* **2024**, 109, B02303. <https://doi.org/10.1029/2003JB002607>.
34. Toda, S.; Stein, R.S.; Richards-Dinger, K.; Bozkurt, S. Forecasting the evolution of seismicity in southern California: Animations built on earthquake stress transfer. *Journal of Geophysical Research* **2005**, 110, B05S16. <https://doi.org/10.1029/2004JB003415>.
35. Storchak, D.A.; Di Giacomo, D.; Bondár, I.; Engdahl, E.R.; Harris, J.; Lee, W.H.K.; Villaseñor, A.; Bormann, P. Public release of the ISC-GEM Global Instrumental Earthquake Catalogue (1900-2009). *Seismological Research Letters* **2013**, 84(5), 810-815, <https://doi.org/10.1785/0220130034>.
36. Storchak, D.A.; Di Giacomo, D.; Engdahl, E.R.; Harris, J., Bondár, I., Lee, W.H.K., Bormann, P.; Villaseñor, A. The ISC-GEM Global Instrumental Earthquake Catalogue (1900-2009): Introduction. *Physics of the Earth and Planetary Interiors* **2015**, 239, 48-63, <https://doi.org/10.1016/j.pepi.2014.06.009>.
37. Di Giacomo, D.; Engdahl, E.R.; Storchak, D.A. The ISC-GEM Earthquake Catalogue (1904–2014): status after the Extension Project, *Earth System Science Data* **2018**, 10, 1877-1899. <https://doi.org/10.5194/essd-10-1877-2018>.
38. International Seismological Centre. ISC-GEM Earthquake Catalogue. **2022**. <https://doi.org/10.31905/d808b825>.
39. USGS Earthquake Hazards Program. Advanced National Seismic System (ANSS) Comprehensive Catalog of Earthquake Events and Products: Various. **2017**. <https://doi.org/10.5066/F7MS3QZH>.

40. Lomax, A.; Savvaidis, A. High-precision earthquake location using source-specific station terms and inter-event waveform similarity. *Journal of Geophysical Research* **2022**, *127*(1), e2021JB023190. <https://doi.org/10.1029/2021JB023190>.
41. Lomax, A.; Henry, P. Major California faults are smooth across multiple scales at seismogenic depth. *Seismica* **2023**, *2*(1), 1-22. <https://doi.org/10.26443/seismica.v2i1.324>.
42. Melgar, D. et al. Sub- and super-shear ruptures during the 2023 M_w 7.8 and M_w 7.6 earthquake doublet in SE Türkiye. *Seismica* **2023**, *2*(3), 1-10. <https://doi.org/10.26443/seismica.v2i3.387>.
43. Kumazawa, T.; Ogata, Y.; Tsuruoka, H. Measuring seismicity diversity and anomalies by point process models: case studies before and after the 2016 Kumamoto Earthquakes in Kyushu, Japan. *Earth, Planets and Space* **2017**, *69*, 169. <https://doi.org/10.1186/s40623-017-0756-6>.
44. Nanjo, K.Z.; Yukutake, Y.; Kumazawa, T. Activated volcanism of Mount Fuji by the 2011 Japanese large earthquakes. *Scientific Reports* **2023**, *13*, 10562. <https://doi.org/10.1038/s41598-023-37735-4>.
45. Ogata, Y. Detection of precursory relative quiescence before great earthquakes through a statistical model. *Journal of Geophysical Research* **1992**, *97*, 19,845-19,871. <https://doi.org/10.1029/92JB00708>.
46. Kumazawa, T.; Ogata, Y. Quantitative description of induced seismic activity before and after the 2011 Tohoku-Oki Earthquake by non-stationary ETAS models. *Journal of Geophysical Research* **2013**, *118*, 6165-6182. <https://doi.org/10.1002/2013JB010259>.
47. Kumazawa, T.; Ogata, Y.; Kimura, K.; Maeda, K.; Kobayashi, A. Background rates of swarm earthquakes that are synchronized with volumetric strain changes. *Earth and Planetary Science Letters* **2016**, *442*, 51-60. <https://doi.org/10.1016/j.epsl.2016.02.049>.
48. Schorlemmer, D.; Wiemer, S.; Wyss, M. Earthquake statistics at Parkfield: 1. Stationarity of b values. *Journal of Geophysical Research* **2004**, *109*, B12307. <https://doi.org/10.1029/2004JB003234>.
49. Shimazaki, K. The almighty earthquake. *Seismological Research Letters* **1999**, *70*(2), 147-148. <https://doi.org/10.1785/gssrl.70.2.147>.
50. Main, I.; Li, L.; McCloskey, J.; Naylor, M. Effect of the Sumatran mega-earthquake on the global magnitude cut-off and event rate. *Nature Geoscience* **2008**, *1*, 142. <https://doi.org/10.1038/ngeo141>.
51. Parsons, T.; Geist, E.L.; Console, R.; Carluccio, R. Characteristic earthquake magnitude frequency distributions on faults calculated from consensus data in California. *Journal of Geophysical Research* **2018**, *123*(12), 10,761-10,784. <https://doi.org/10.1029/2018JB016539>.
52. Schwartz, D.P.; Coppersmith, K. J. Fault behavior and characteristic earthquakes: examples from Wasatch and San Andreas fault zones. *Journal of Geophysical Research* **1984**, *89*, 5681-5698. <https://doi.org/10.1029/JB089iB07p05681>.
53. Emre, Ö.; Duman, T.Y.; Olgun, S.; Elmaci, H.; Özalp, S. 1:250,000 Scale Active Fault Map Series of Turkey, Gaziantep (NJ 37-9) Quadrangle. *Serial Number: 38, General Directorate of Mineral Research and Exploration, Ankara-Turkey* 2012.
54. Wessel, P.; Smith, W.H.F.; Scharroo, R.; Luis, J.F.; Wobbe, F. Generic Mapping Tools: improved version released. *EOS, Transactions, AGU* **2013**, *94*(45), 409-410. <https://doi.org/10.1002/2013EO450001>.

Disclaimer/Publisher's Note: The statements, opinions and data contained in all publications are solely those of the individual author(s) and contributor(s) and not of MDPI and/or the editor(s). MDPI and/or the editor(s) disclaim responsibility for any injury to people or property resulting from any ideas, methods, instructions or products referred to in the content.